



A short review on selective laser melting of H13 steel

Jintao Wang¹ · Shouping Liu¹ · Yunpeng Fang¹ · Zhongrui He¹

Received: 21 December 2019 / Accepted: 2 June 2020 / Published online: 9 June 2020
© Springer-Verlag London Ltd., part of Springer Nature 2020

Abstract

In this review, the present situation of H13 tool steel formed by selective laser melting (SLM) is introduced in detail. This review shows the current academic exploration and achievements in this field through the three aspects of microstructure, defects, and mechanical properties. We presented the distribution of the alloy elements and the different crystal morphology. We summarize the main defects of this alloy prepared by SLM from three aspects: the rough surface, cracks, and low density. The mechanical properties of H13 tool steel formed by SLM are also introduced. All in all, it shows a wide application prospect of SLMed H13 steel.

Keywords SLM · 3D print · AM · H13 steel · Defects

1 Introduction

Additional manufacturing (AM, 3D printing) is an advanced technology in the manufacturing industry. This technology has been used in aerospace, biomedical engineering, and other different fields, and its latest development has brought great social value for its future [1–3]. It possesses the advantages of facilitating structural optimization, allowing realizing intricate structures that can hardly be made by conventional forging or casting processes [4, 5]. Now, layered manufacturing of non-metallic parts with one or two materials has become a mature topic. It has been successfully proved that the single material metal parts manufactured by LENSTM, SLS, SLM, and other technologies have been applied [6–10]. The SLM process starts with an orthopedics CAD model that contains information about the areas to be melted in separate layers. SLM is a fabrication process where 3D model data is revolved into a 3D near-net functional component [11–13]. The standard file format for collaboration between design software and printers is STL. An STL file uses triangular faces to approximate the surface of an object. The smaller the triangular surface, the higher the surface resolution. Ply is a kind of scanner for 3D files generated by scanning. VRML or WRL files generated by ply are often used

as input files for full-color printing. A certain amount of powder is placed on the base plane and the powder layered by blades and roller. A high-power laser with a distinctive pattern melts the powder and creates 3D parts (Fig. 1). Powder particles absorb energy when the high energy laser beam irradiates on the powder bed. And transient temperature field with high temperature and rapid cooling rate is the characteristic of the SLM, which will affect the microstructure and mechanical properties of the specimens [2, 14–17].

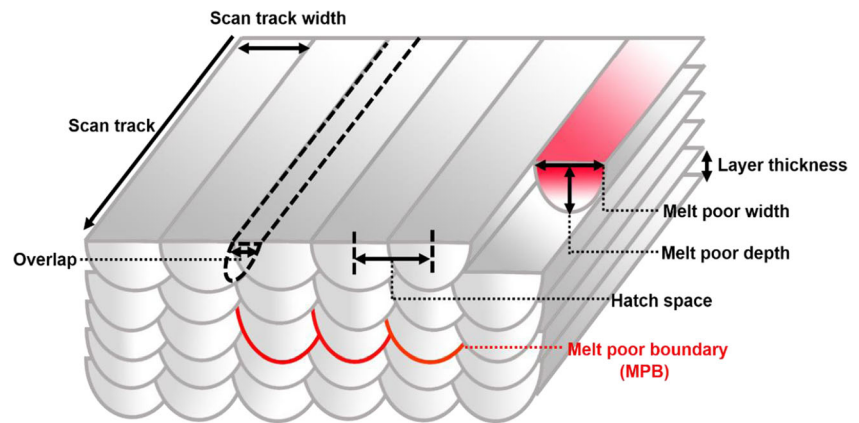
H13 steel is a C-Cr-Mo-Si-V steel, which is widely used in the world. At the same time, many scholars in various countries have carried out extensive research on it and are exploring the improvement of chemical composition. H13 tool steel has high hardenability due to its high carbon content and alloy elements, so it has complex processing properties. H13 steel is usually used to make injection molds to high-working temperature and thermal fatigue, because of its excellent performance and low cost [15–19]. Generally, the way of strengthening H13 steel is nitriding and boronizing [20–22]. And, the martensite structure of H13 steel after quenching is lath martensite + a small amount of lamellar martensite + a small amount of retained austenite. As a kind of die steel, with the demand of modern society for workpiece model more diversified and more complex, the original casting method has been unable to meet this demand. Now, many researchers point out that the preparation of H13 steel by SLM can be utilized as a new strengthening method [23–25].

Some properties of H13 steel produced by SLM are better than those of H13 steel made by FST (forging, specialized annealing, thermal refining). Bo pointed out that the tensile

✉ Jintao Wang
1324968548@qq.com

¹ College of Materials Science and Engineering, Chongqing University, Chongqing 400044, China

Fig. 1 A schematic diagram of the scanning strategy of the SLM process (adapted from [14])



strength of SLMed H13 is 1909 MPa, and that of FSTed-H13 steel is 1962 MPa (Fig. 2). However, the elongation of SLM (12.4%) is three times that of FST (4.4%). Because of the two-phase structure, the specimens have the characteristics of continuous yield and rapid initial hardening [6, 15, 26, 27].

In SLM process, the mechanical properties of printed metal parts are highly dependent on intricate printing parameters. Therefore, process parameters are very important for the manufacturing of H13 tool steel [14, 28–30]. Therefore, it is necessary to summarize the SLMed H13 process parameters, micromorphology, properties, and defects.

2 Microstructure

2.1 Microstructure in an SLMed state

SLM has the nature of rapid melting and solidification compared with traditional manufacturing, so it has obvious advantages. High cooling rate induced large thermal supercooling and dynamic supercooling to the molten pool. The high

nucleation rates refine the microstructures significantly due to the substantial undercooling degree within the pool [19, 31, 32]. The microstructure from cross sections along the build direction shows columnar grains oriented along the building direction (Fig. 3a). Because of the heat conduction, the grains elongate along the direction of laser scanning. Besides, the grain size of the traditional manufacturing specimens is greater than that of the SLM specimens. And the anisotropy between grains of the FST specimens is higher than that of the SLM specimens [15]. Most of the grains are isolated by high-angle grain boundaries [33]. The amount of low-angle grain boundaries in H13 produced by SLM is larger than that in H13 produced by FST (Fig. 3 c and d). In addition, the crystallographic characteristics of lath martensite SLMed H13 are revealed by high-angle grain boundary mapping (Fig. 3b): parallel laths and a large number of dislocations. Because adjacent cells generally have almost the same crystallographic orientation, these cells in IPF (inverse pole figure) were no grains [34]. Owing to the different cooling rates in different regions of the cube and the cyclic thermal effect, some martensitic structures will be decomposed into α -Fe and carbides [35, 36].

As-SLMed H13 microstructure includes martensite and a large amount of austenites (RA) [37]. It is pointed out that H13 treated by SLM consists of martensite and a large number of retaining austenites (10–15%) [37–39]. There are a lot of retained austenites in H13 tool steel processed by SLM. The proportion of retained austenite in H13 steel produced by SLM is larger than that in H13 steel produced by FST [15]. Because of the high cooling rate and subsequent supercooling in SLM process, the solidification of the molten pool is considered to be carried out without separation, which leads to uniformity of chemical composition [40]. However, due to the high cooling rate of H13 steel produced by SLM, the distribution of Cr, Mo, and V during solidification is restrained [16]. Enrichment of heavy metals is caused by rapid solidification. The segregated heavy alloy elements at the boundary of the molten pool result in cellular/dendritic microstructure of H13 steel [37]. Similarly, due to the rapid cooling, the carbide

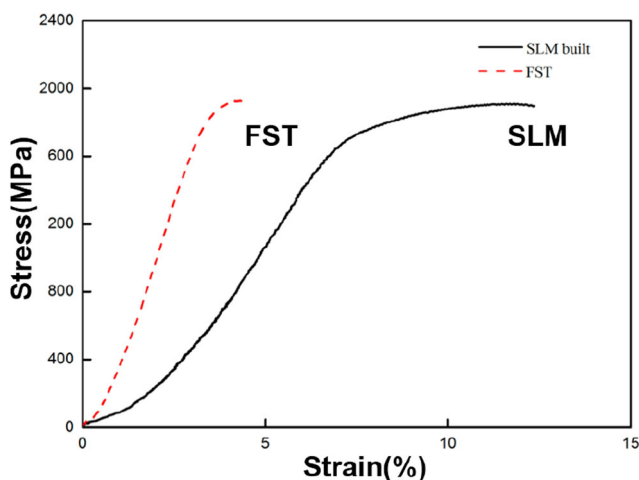


Fig. 2 Mechanical properties of SLM and FST, and stress-strain curves under different treatments [15]

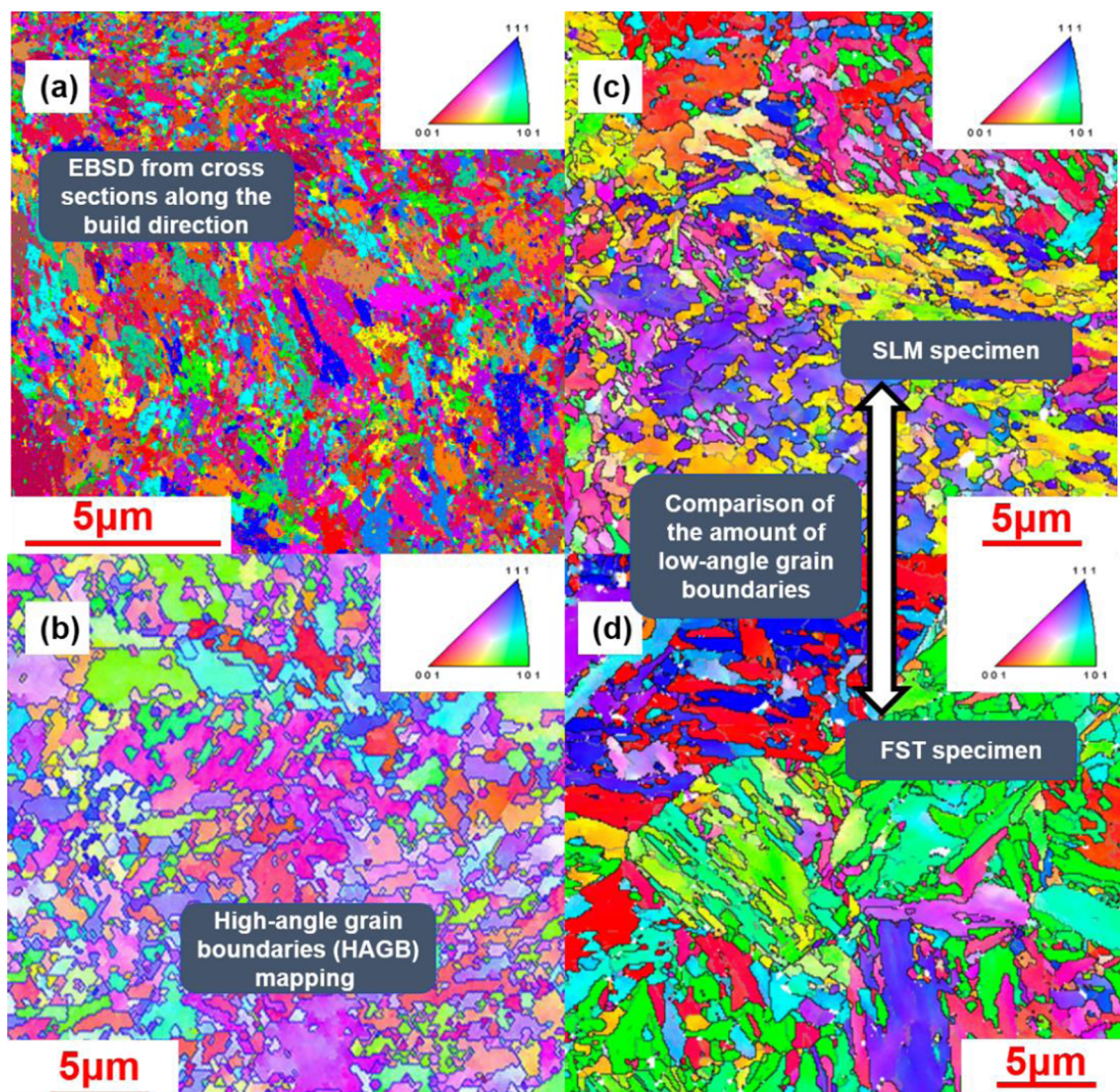


Fig. 3 Electron backscatter diffraction (EBSD) maps of H13 steel. **a** Grain orientation maps (along the build direction) $P = 300$ W, $v = 1000$ mm/s [18]. **b** Inverse pole figure (IPF) of SLMed H13 specimens, $P = 280$

$W, v = 980$ mm/s [41]. **c** EBSD analysis of SLMed H13 steel. **d** EBSD analysis of FSTed-H13 steel [15]

cannot diffuse in time, which promotes the formation of martensite rather than ferrite.

3D APT (atomic probe tomography) is carried out to analyze the distribution of V, Cr, Mn, and Mo atoms, which is segregated in the edge of the C-rich region and helps to prevent the diffusion of C [14, 40, 41]. The carbide-stabilizing elements aggregate as cellular substructure, which occurs during the rapid solidification of SLM process (Fig. 7a) [41]. The high concentration of the C atom in the local region obtains the stabilization of austenite phase at room temperature, because C atom is a strong austenite stabilizer. Higher laser energy density results in lower porosity and higher retained austenite volume.

Most of the grain diameters of as-SLMed H13 are a few microns (about 5 μm). H13 steel produced by SLM has three distinct types of grain structures, specifically columnar grain,

fine cellular grain, and coarse cellular grain. This results in the different temperature gradients at the solid–liquid interface and the different growth rates during solidification (Fig. 4) [1]. Generally, the microstructure in the center of the molten pool is relatively coarse [36]. The columnar grains have the exact same orientation as the laser scanning direction [33, 42]. Owing to the technical characteristics of SLM “layer-layer” deposition, there is a bright and dark etching zone and “track-track” molten pool boundaries (MPBs) in the microstructure [41, 43, 44]. The number of interlaminar fine cracks increases with the increase of energy density.

The lattice constants of α -Fe solid solution of H13 steel manufactured by SLM are distorted, and the lattice constants are large. The rapid heating–solidification cycle in the SLM process leads to the formation of cellular grains and the uniform dispersion of alloy elements [33].

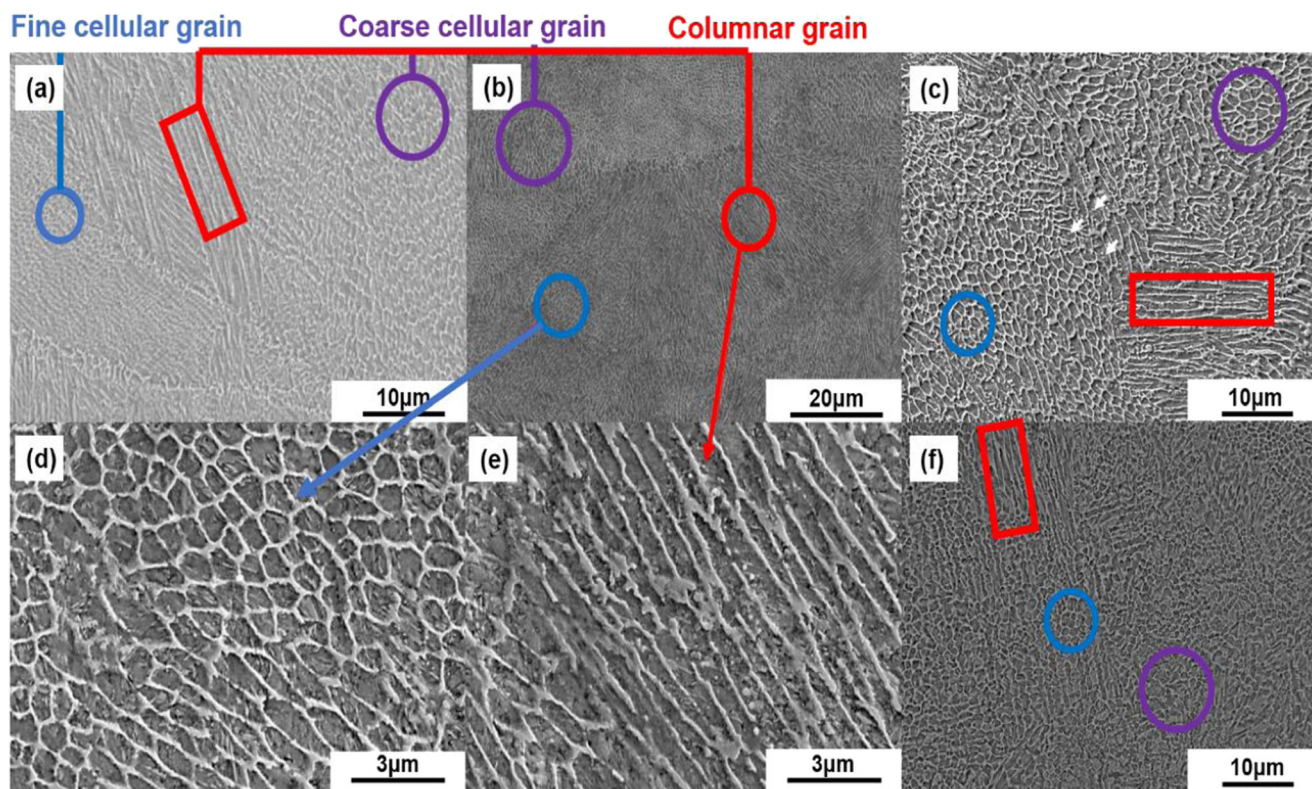


Fig. 4 SEM images of the additively manufactured H13 high-strength steel samples. **a** 175 W, 725 mm/s, preheated to 200 °C [1]. **b** $P = 300$ W, $v = 1000$ mm/s [18]. **c** $P = 100$ W, $v = 250$ mm/s [19]. **d** Fine cellular

grain, $P = 300$ W, $v = 1000$ mm/s [18]. **e** Columnar grain, $P = 300$ W, $v = 1000$ mm/s [18]. **f** $P = 150$ W, $v = 250$ mm/s [37]

During the solidification process, dendrite was formed in a short time. Volute elements gathered at the grain boundary, forming micro segregation and cellular structure. And the number of fine cellular grains increases with the increase of building height, because the influence of heat flux decreases, and “competitive growth” becomes favored [37, 45, 46]. And “cross-hatching” (Fig. 6a) laser scanning strategy can induce more subtle cellular grains, resulting in a more isotropic microstructure [47].

Low volumetric laser energy density results in the formation of columnar grains [28]. The scanning method shown in Fig. 6b (rotation angle 67°) usually destroys the columnar structure defined in SLM samples [15]. The first layer is reheated and solidified during the formation of the second layer, resulting in coarse cellular particles in the first layer (Fig. 5). Changing the volumetric laser energy density (Eq. 1) is the way to prevent coarse grains.

$$E_v = \frac{P}{v \times h \times t} \quad (1)$$

where E_v denotes the volumetric laser energy density (J/mm³); P denotes the laser power (W); v denotes the

scanning speed (mm/s); h denotes the hatch spacing (mm); and t denotes the layer thickness (mm).

2.2 Microstructure after heat treatment

Heat treatment of H13 steel usually includes quenching and tempering (Fig. 6). After quenching, the sample shows a large number of carbides for precipitates evenly distributed among the grains (Fig. 7) [18]. And, cellular/dendritic solidification is removed by homogenization. Moreover, the precipitates in the as-SLMed microstructure also disappeared, confirming that the effect of inherent tempering in the SLM process was eliminated by quenching [48]. This is also consistent with the absence of retained austenite after quenching (less than 2%), which sets the best conditions for the upcoming tempering (i.e., uniform structure and hardness, and no retained austenite).

After tempering, the retained austenite is transformed into a mixture of cementite and ferrite, and the cellular substructure caused by segregated of heavy elements gradually dissolves into the matrix to form flat ferrite, and then spherical carbide is precipitated (Fig. 8). Generally, the microstructure of tempered H13 steel is composed of tempered martensite, and it is dispersed with very slight secondary carbide. However, the

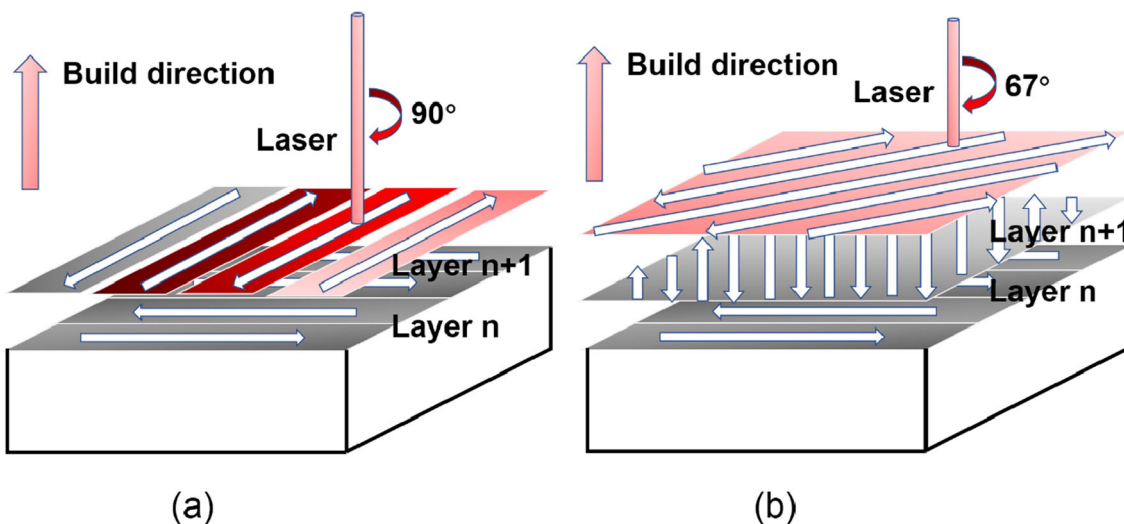


Fig. 6 Several scanning strategies. **a** “Cross-hatching” scanning strategy (the rotation of the scanning direction by 90°). **b** The rotation of the scanning direction by 67°

honeycomb structure will be restored, and the carbide network will be formed [38, 41, 48].

3 Defects

3.1 Cracks

Cracking is a common defect in additive manufacturing parts, which seriously limits the performance of parts. There are several reasons for the formation of cracks at as-SLMed H13 steel. First, the collision of the specimens and the powder recoating machine will cause cracks in the specimens. And, high thermal stresses associated with the manufacturing process of SLMed H13 can cause cracking and delamination from the base plate (Fig. 9). Balling effect also results in cracks (Fig. 10) [18, 49, 50].

The upper layer of solid matrix will expand due to high temperature, while the lower solidified layer will limit this expansion. This makes the upper layer of the substrate

produces a significant compressive stress, which may be higher than the yield strength of the material and lead to plastic deformation of the upper layer. When the plastic deformation layer cooling is present, their state is transformed into residual tensile stress. These residual stresses may cause cracking of the part. When the yield strength is attained, the compressive stress causes plastic deformation in the upper layer. In addition, the melted top layer tends to shrink owing to thermal shrinkage. This deformation is again blocked by the lower layer, thus introducing tensile stress into the uppermost layers [20, 50]. Many researchers have shown that preheating the substrate to reduce steep thermal gradients could prevent cracks caused by thermal stress [24, 35, 51]. Preheating at 200 °C usually helps to increase relative density and eliminate crack formation [18]. Balling effect is described in the “A rough surface” section.

3.2 A rough surface

Surface roughness is one of the most important features of complex geometry in AM production. Surface roughness is insufficient melting of the powder particles on the powder bed and balling effect [52, 53].

The reasons for balling effect are described as follows:

- (1) When the laser power is above a certain value (depending on the different powders), there is evaporation and splashing into the molten metal pool; so in the absence of liquid metal, there are many pores. At the same time, the splashed liquid will fall into the molten pool and form a small spheroidizing area (Fig. 11). Excessive laser energy input causes a steep temperature gradient between the center and the edge of the entire surface, resulting from

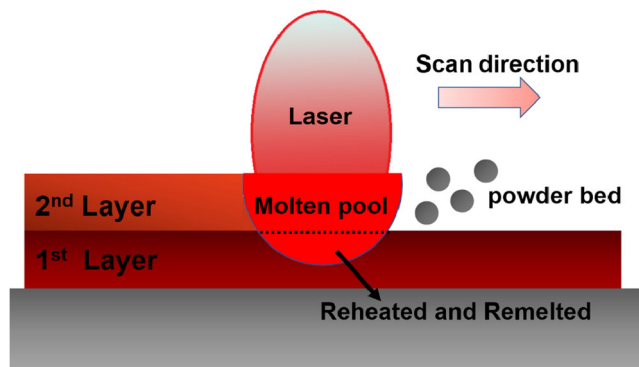
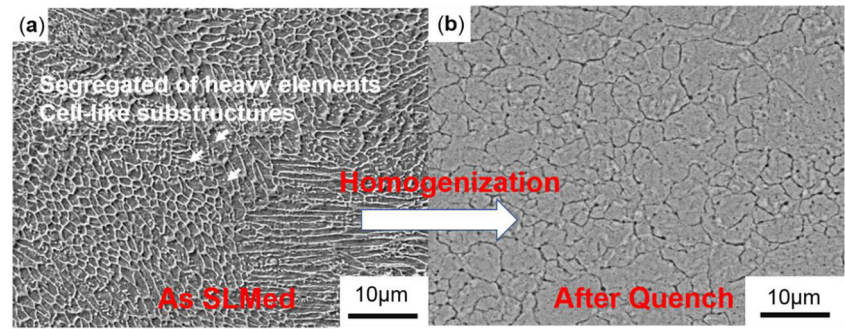


Fig. 5 Schematic diagram of remelted area

Fig. 7 Homogenization of heavy elements during quench. **a** SEM micrographs of as-SLMed microstructure. **b** SEM micrographs of quenched microstructure, heated 1020 °C, cooled at 40 °C/min [19]



the surface tension gradient and the resulting Marangoni effect [28]. As a result of the Marangoni effect, the melt has a tendency to flow radially inward to the center of the melt pool rather than outwards on the surface below [54, 55].

- (2) Low laser power also causes a balling effect. Laser sintering is a line-by-line process which the powder particles absorb energy through bulk-coupling and powder-coupling mechanisms [44, 58]. The solidus

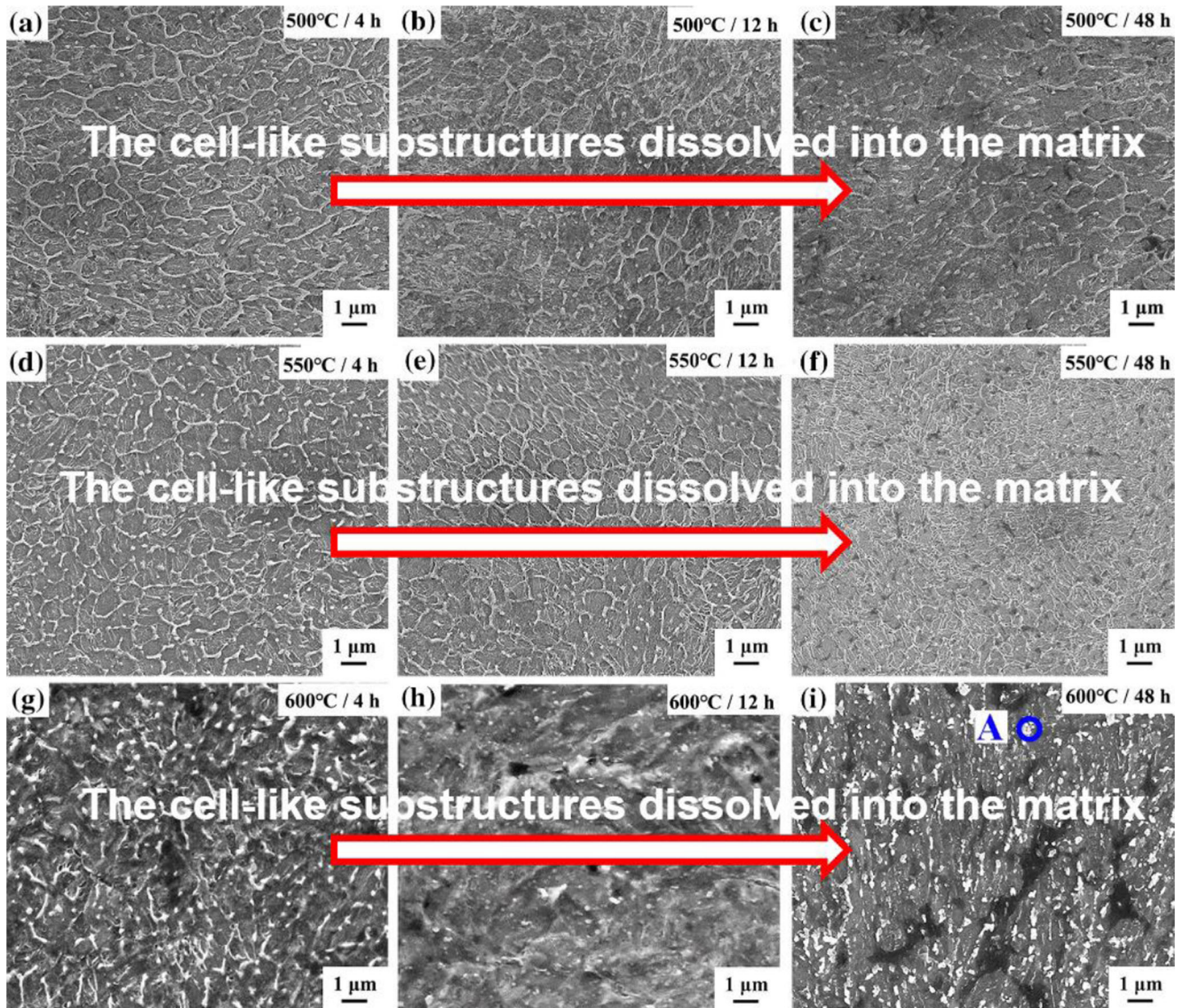


Fig. 8 SEM images of SLMed H13 specimens [41]

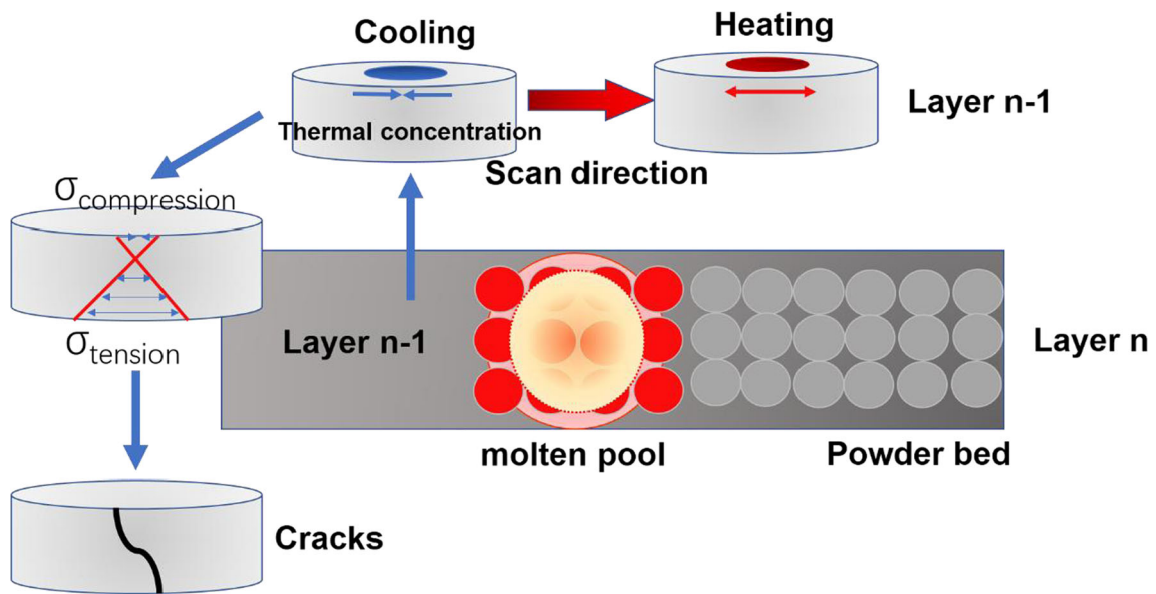


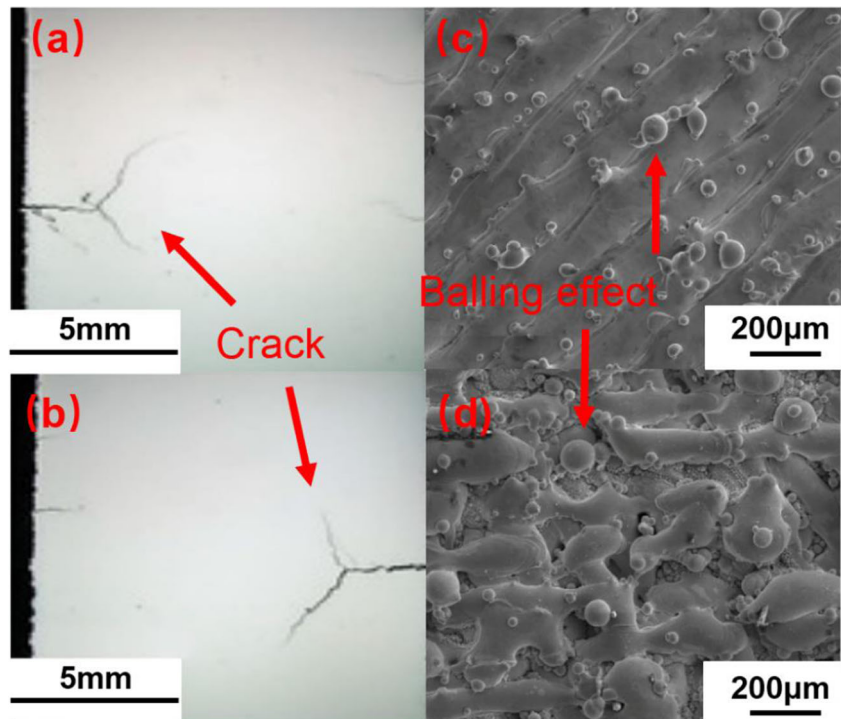
Fig. 9 Thermal stresses in SLM

sintering temperature decreases with the laser power for a gave scan speed, which results in the amount of liquid reducing. This hinders the rheological behavior of liquid and causes the rearrangement of liquid flow and particles more grim [45, 58]. Therefore, the molten material in the focused spot area of each point tends to aggregate into a single coarsening sphere, whose diameter is approximately the diameter of the

laser beam (Fig. 12). And sintering necks unformed with a limited liquid amount, which is caused by low laser power [31, 52].

- (3) With the increase of scanning speed, the melt droplet is easier to splash. Laser sintering at high scanning speed often causes the melt form into a continuous

Fig. 10 Optical micrographs of H13 produced by SLM. **a** The laser power of 300 W, scanning velocity of 1000 mm/s. **b** $P = 300$ W, $v = 800$ mm/s. **c** $P = 300$ W, $v = 1000$ mm/s. **d** $P = 300$ W, $v = 1000$ mm/s [18]



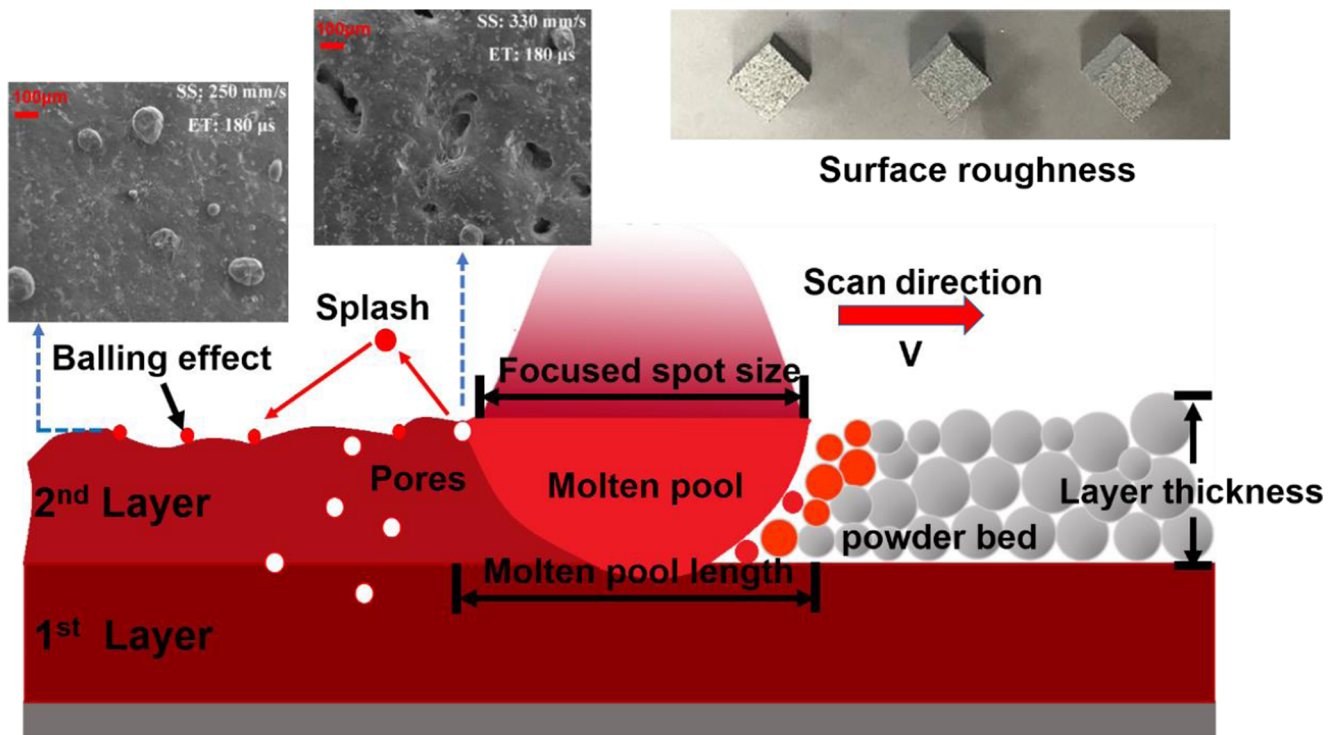


Fig. 11 Balling effect caused by high laser power (adapted from [18, 56, 57])

cylindrical melt, and because the residence time of laser spot on each focused spot area is very short, so the molten sintering track is short. The molten

sintering track is highly unstable at high scanning speed, and the surface energy of the liquid trajectory will decrease continuously to obtain the final

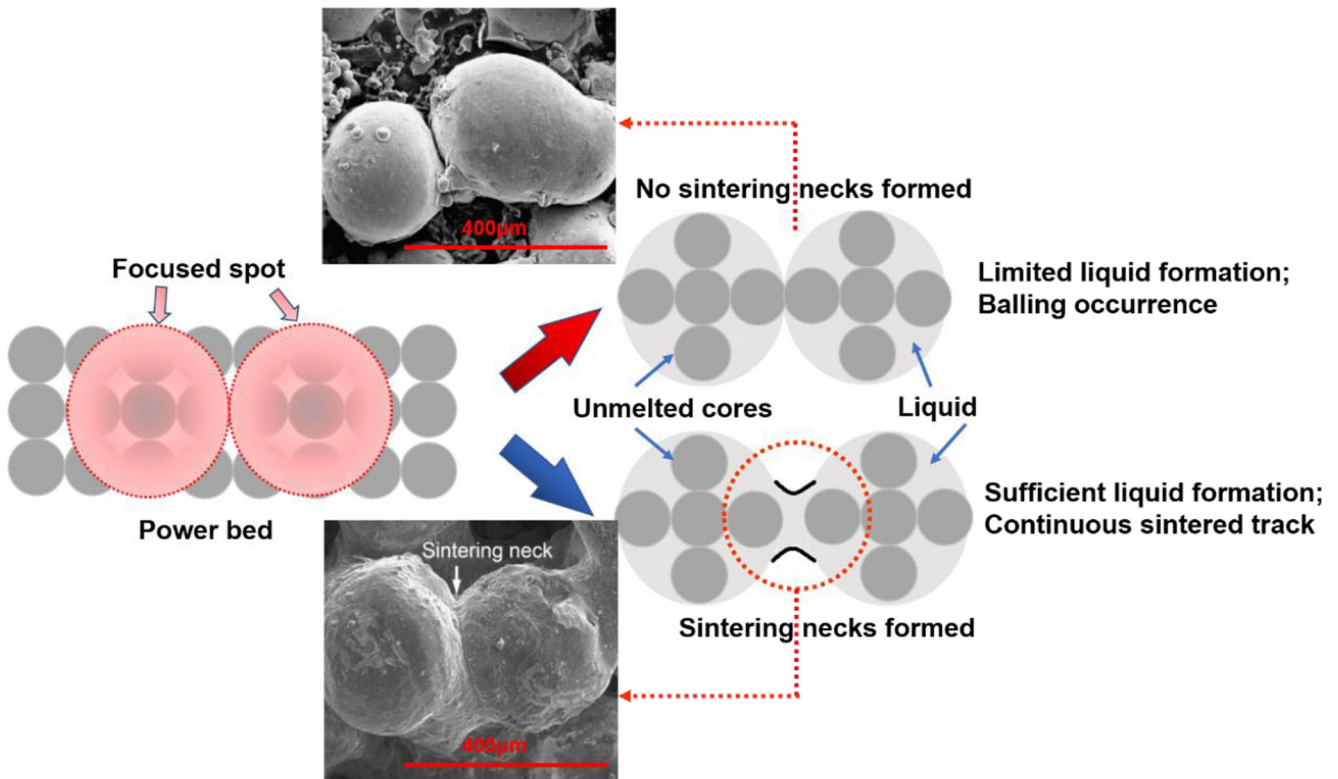


Fig. 12 Balling effect caused by low laser power (adapted from [52])

equilibrium state. Surface energy reduction causes numerous small liquid droplets to splash from the surface of the molten track. Simchi believes that the laser scanning speed has a significant effect on the capillary instability of the liquid trajectory. The increase of scanning speed leads to the decrease of laser input energy density, which leads to the decrease of working temperature and melting path diameter with the increase of scanning speed. Therefore, the equilibrium state of the molten cylinder was breaking up, thereby producing longitudinal cracks in the finally solidified tracks (Fig. 13) [50, 52].

- (4) Slow laser scanning also results in a balling effect. The interaction time between laser and powder is relatively long with the slow scanning speed, which leads to an excessive local liquid. Due to the too large molten pool, the powders around the molten pool are sucked into the pool, resulting in the shortage of powder in the original position. Thereby, the sample shows low density and has obvious pores [55, 56].

The cracks and surface roughness caused by the balling effect (Fig. 14) are the major macroscopic characteristics. H13 steel specimens generated by SLM obtain smooth surface and structure without cracks lying incorrect laser power and

laser speed. Bo Ren [15] puts up forward that the optimum process parameters are a laser power of 170 W, scanning speed of 400 mm/s in accordance with the maximum relative density of 99.2%. In conclusion, macroscopic characteristics of H13 produced by SLM lie in the correct process parameters, mainly laser scanning speed and laser power.

Additive manufacturing allows the production of parts directly from the numerical data of computer-aided design (CAD) model. It has significant advantages, which can form complex structural parts freely, and its design time is short. For example, in reference [1], SLM is used to prepare steel pipe profiles, and in reference [36], SLM technology is used to make high-precision blades. According to the requirements of forming parts, there are many scanning strategies (Fig. 6) [1]. The typical process defects associated with SLMS in macroscopic characteristics include distortion, delamination, and porosity, but a more important problem is the balling effect (Fig. 5) [52]. Marangoni effect is presented as the mass transfer along an interface between two fluids due to a gradient of the surface tension [28, 50].

Balling effect will lead to cracks and surface roughness, which is disastrous for a mold (H13 steel is usually used to make molds). Because SLM is a layer by layer additive manufacturing process, the balling effect hinders the uniform deposition of fresh powder on the previously sintered layer, and often leads to porosity, even results in the edges of the

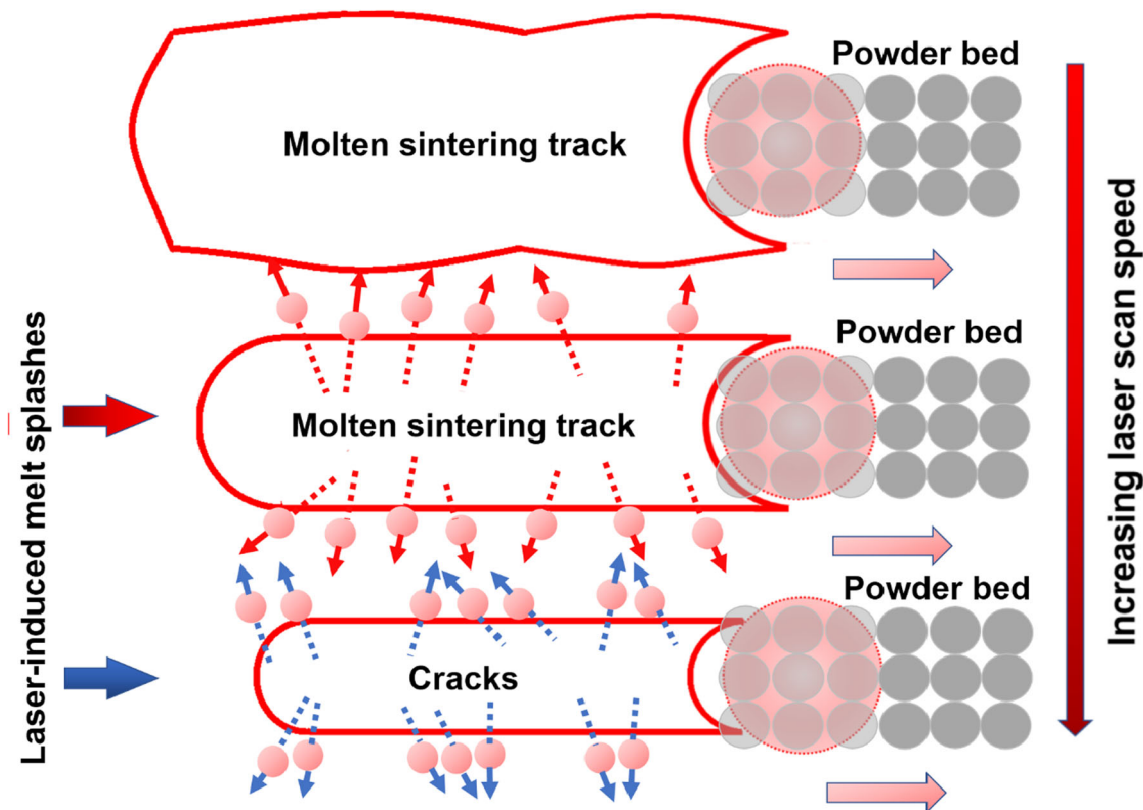
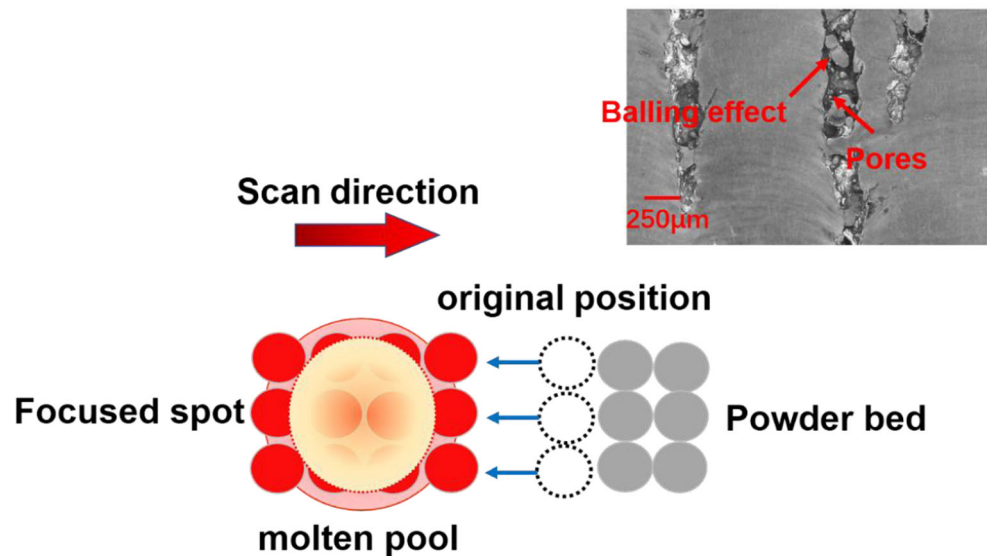


Fig. 13 Schematic diagram of balling effect caused by high laser scanning speed

Fig. 14 Balling effect caused by slow laser scanning speed (metallograph from [28])



printing parts warping from parts, which is a phenomenon called layer spallation [7, 15, 50, 56].

3.3 Low density

The density of H13 steel produced by SLM increases with the increase of volumetric laser energy density until E_v reaches about 60 J/mm^3 . The maximum density is about 99.7%. Increasing the scanning speed at the same power level will have a negative effect on the density of H13 specimens [18, 59]. In addition, by increasing the laser energy density per unit volume, the temperature rise of the readily solidified layer caused by the heat transfer from the solidified layer to the matrix will increase [46, 60]. The density of H13 steel also can be enhanced by laser remelting. And through the second laser scanning, the pores on the top of the molten pool are effectively closed, but the pores under the molten pool cannot be removed by the second laser scanning [33, 61, 62].

Hot isostatic pressing (HIP) post-treatment was applied to improve the density of the SLMed H13 steel [63, 64]. In the research of Bandar, the relative density was 80.5% before HIP treatment and increased to about 98.2% after HIP treatment. HIP high-temperature treatment allows the diffusion of elements, resulting in the coexistence of stability and equilibrium phases, and the formation of more homogeneous materials [33].

3.4 Residual stresses

Generally, the initial local geometric defect of the H13 test piece ranges from 0.03 to 0.31 mm [1]. SLMed H13 specimens have lower mechanical properties under the completion condition, and compared with the traditional production, the tensile and fatigue behavior of H13 samples produced by

SLM in mechanical test show that the tensile strength of the samples produced by SLM is 30% lower than that of traditional production. This is caused by residual stress [49, 65, 66].

The steel base plate used in SLM processes usually needs to be thick and strong enough to resist the probable 1 deformation of the manufactured specimens, besides, the finished parts need to be annealed to relieve stress. The range of residual stress of the SLMed H13 sample is 900–1500 MPa [35, 53, 67]. The residual stress level of the specimens can be seen as the result of the equilibrium between the transformation and the strain. Martensitic transformation is part of the key reasons for high-level compressive residual stress.

Stress relief provided for H13 is usually annealed for 2 h in the temperature range of 600–650 °C [35, 49] (Table 1).

4 Mechanical properties

Microhardness and tensile test are classic methods to evaluate the mechanical properties of SLMed H13 tool steel [17, 40]. Owing to the existence of a large number of martensites, the hardness is evenly distributed in SLMed H13 [18]. The residual stress caused by the high solidification rate (10^6 – 10^8 k/s) in the SLM process also is beneficial to enhance the hardness [41]. It is noted that the hardness of SLMed H13 steel is easily affected by strain rate [40]. Van et al. refer that “the strain-rate sensitivity exponent ($m = 0.022$) of SLMed H13 steel indicated that the nanoindentation hardness increased in a range of 8.41–9.18 GPa with an increase in the strain rate ranging from 0.002 to 0.1 s^{-1} ”. And, nanoindentation strain-rate sensitivity values were 0.022, 0.019, 0.027, 0.028, and 0.035 for SLMed H13 steel at laser scan speed of 100, 200, 400, 800, and 1600 mm/s, respectively. The SLMedH13 at 200 mm/s laser scan

Table 1 SLM process parameters and as-SLMed H13 steel mechanical properties

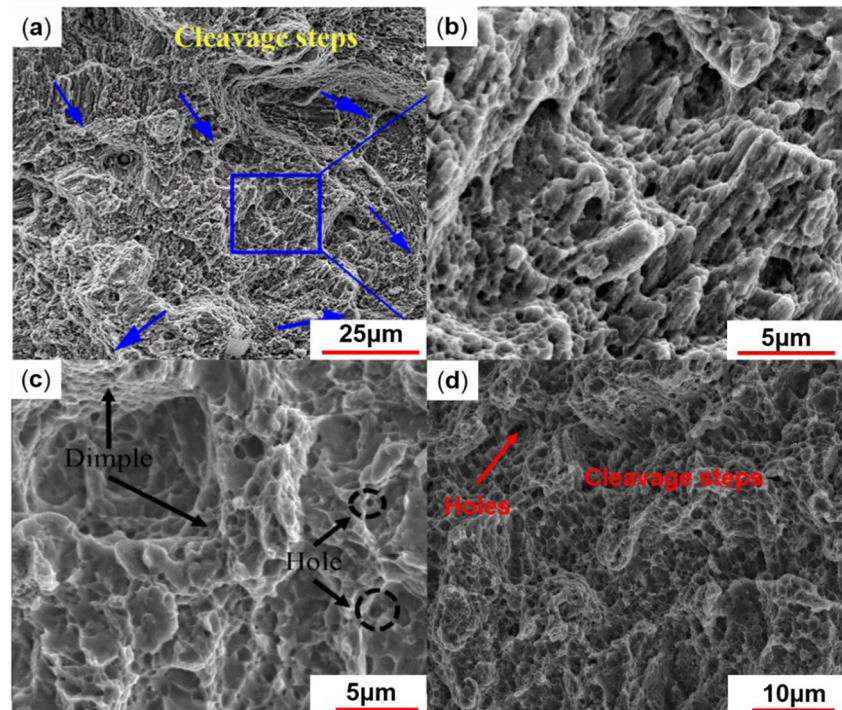
Process parameters	Hardness (HV)	Tensile strength (MPa)	Elongation at break (%)	Reference
$P = 300$ W, $v = 400$ mm/s, hatch spacing = 50 μm preheating of 200 $^{\circ}\text{C}$,	706 ± 147	835 ± 23	4.1 ± 2.3	[24]
$P = 300$ W, $v = 400$ mm/s, hatch spacing = 50 μm without preheating	894 ± 48	1236 ± 178	4.1 ± 1.2	[24]
$P = 400$ W, $v = 725$ mm/s, hatch spacing = 100 μm , layer thickness = 30 μm , preheating of 200 $^{\circ}\text{C}$	715	1025	1.7	[1]
$P = 280$ W, $v = 980$ mm/s, hatch spacing = 120 μm , layer thickness = 40 μm	575	1026 ± 5	12.9 ± 0.96	[41]
$P = 170$ W, $v = 400$ mm, hatch spacing = 100 μm , layer thickness = 40 μm	561	1909	12.4	[15]
$P = 90$ W, $v = 200$ mm/s, hatch spacing = 80 μm , layer thickness = 25 μm	-	1700	1.6	[14]
$P = 100$ W, $v = 200$ mm/s, hatch spacing = 100 μm , layer thickness = 30 μm	506	-	-	[65]
$P = 100$ W, $v = 250$ mm/s, hatch spacing = 120 μm , layer thickness = 50 μm	748.04 ± 27.61	-	-	[33]
$P = 175$ W, $v = 750$ mm/s, hatch spacing = 120 μm , layer thickness = 30 μm	-	1550–1650	2–2.25	[67]
$P = 175$ W, $v = 600$ mm/s, hatch spacing = 120 μm , layer thickness = 30 μm , preheating of 200 $^{\circ}\text{C}$	-	1003 ± 9	1.7 ± 0.6	[49]

speed shows the highest potential for advanced tool design [40]. Hardness of the SLMed H13 specimens is higher than that of the traditional manufactured H13 specimens. This high initial hardness is lying in the grain refinement effect produced by rapid solidification and the existence of the martensite phase which is favorable for high hardness [33]. The SLMed H13 samples' hardness values at different strain rates were greater than that of the H13 prepared by FST [49, 64, 68]. And the hardness increases with the nanoindentation strain rate, which means that the brittleness of the SLMed H13 steel

would increase at higher strain rates [40]. HIP treatment also can increase the hardness [33].

In the tensile test, hardening is observed [67], which is linked to the transformation from metastable austenite to martensite. The stress-strain behavior of SLMed H13 high-strength steel is very different from that of conventional high-strength steel [1]. All tensile specimens failed due to sudden fracture without necking [1, 15, 39, 41]. Tensile fracture morphology of SLMed H13 shows typical brittle fracture characteristics, with two different regions: shear lip and fiber

Fig. 15 SEM images of the as-SLMed H13 steel fracture surface. **a** [15]. **b** [15]. **c** [41]. **d** [60]



region (Fig. 15). It can be observed that there are cleavage steps in the river pattern, which indicates that the fracture mechanism is quasi fracture. In the process of tension, cracks mainly appear in small shallow pits and deformation pits, and scattered holes become the source of these cracks. At the same time, the interface defect between lath martensite and retained austenite is also the source of crack. Martensitic grains of SLM samples are fine, and the second phase particles do not precipitate, so the fracture occurs along the grain boundary. Micropores propagate in the direction of strain cracks to retain austenite or along the boundaries of martensite particles [15, 37, 41, 60].

The high texture microstructure in the building direction leads to the phenomenon that the longitudinal tensile strength is higher than the transverse tensile strength [45]. The growth direction and the ratio of grain length to width lead to anisotropic behavior, which will affect the mechanical properties of SLMed H13 [65, 69, 70]. Jungsub refers that the large cluster with unmelted pores behaved as crack initiation sites which led to the degradation of mechanical property. It is confirmed that fine grains and no second-phase precipitation determine the strength and plasticity of SLM samples [15, 71, 72]. At present, there is not a complete conclusion in the study of the influence of process parameters on mechanical properties, and there is a lack of comprehensive research on the impact of process parameters on mechanical properties.

A slight increase in the mechanical properties was observed as a result of the grain coarsening and agglomeration of the TiB₂ nanoparticles in the H13 matrix [33].

5 Summary and outlook

In this brief review, previous studies on H13 steel by SLM were summarized. Characteristics of SLM manufacturing complex geometry provide a greater prospect for H13 steel:

- (1) As-SLMed H13 steel is composed of martensite and maintained austenite. Heavy alloy elements segregate around the C-rich region to form a cell-like substructure.
- (2) H13 steel formed by SLM has three distinct types of grain structures, namely columnar grain, coarse cellular grain, and fine cellular grain.
- (3) Tempering and quenching heat treatment can make the cell-like substructure dissolve into the crystal cell and narrow the residual austenite. Annealing can remove the residual stress.
- (4) Defects in SLMed H13 steel are cracked, rough surface, residual stress, and density.
- (5) Hardness of H13 is related to stress-strain sensitivity exponent. Tensile fracture morphology of SLMed H13 shows typical brittle fracture characteristics.

For future research of SLMed H13 steel, we put forward the following academic explorations:

- (1) Reinforced steel composites (such as TiB₂/H13) show a serious prospect in SLM manufacturing.
- (2) Further enhance the print strength by increasing the density of SLMed H13 steel.
- (3) Explore heat treatment systems matching with SLM technology for reducing print deformation and getting a more precise design.
- (4) Explore polishing technology matching with SLM technology to make SLMed H13 steel printing get a smoother surface.

Acknowledgments In particular, I would like to thank Dr. Chaoqun Zhang of Shanghai Jiaotong University for his help.

Compliance with ethical standards

Conflict of interest The authors declare that they have no conflict of interest.

References

1. Yan J-J, Chen M-T, Quach W-M, Yan M, Young B (2019) Mechanical properties and cross-sectional behavior of additively manufactured high strength steel tubular sections. *Thin-Walled Struct* 144:106158
2. Brandl E, Heckenberger U, Holzinger V, Buchbinder D (2012) Additive manufactured AlSi10Mg samples using Selective Laser Melting (SLM): microstructure, high cycle fatigue, and fracture behavior. *Mater Des* 34:159–169
3. Louvis E, Fox P, Sutcliffe CJ (2011) Selective laser melting of aluminium components. *J Mater Process Technol* 211(2):275–284
4. Yan J, Zhou Y, Gu R; Zhang X, Quach W.-M., Yan M (2019) A comprehensive study of steel powders (316 L, H13, P20 and 18Ni300) for their selective laser melting additive manufacturing. *Metals* 9, (1).
5. Mazur M (2016) SLM additive manufacture of H13 tool steel with conformal cooling and structural lattices. *Rapid Prototyp J* 22(3): 504–518
6. Al-Jamal OM, Hinduja S, Li L (2008) Characteristics of the bond in Cu–H13 tool steel parts fabricated using SLM. *CIRP Ann* 57(1): 239–242
7. Childs THC, Hauser C, Badrossamay M (2004) Mapping and modelling single scan track formation in direct metal selective laser melting. *CIRP Ann* 53(1):191–194
8. Rombouts M, Kruth JP, Froyen L, Mercelis P (2006) Fundamentals of selective laser melting of alloyed steel powders. *CIRP Ann* 55(1):187–192
9. Kruth JP, Froyen L, Rombouts M, Van Vaerenbergh J, Mercelis P (2003) New ferro powder for selective laser sintering of dense parts. *CIRP Ann* 52(1):139–142
10. Delgado J, Ciurana J, Rodríguez CA (2011) Influence of process parameters on part quality and mechanical properties for DMLS and SLM with iron-based materials. *Int J Adv Manuf Technol* 60(5-8):601–610
11. Kadirgama K, Harun WSW, Tarlochan F, Samykano M, Ramasamy D, Azir MZ, Mehboob H (2018) Statistical and

- optimize of lattice structures with selective laser melting (SLM) of Ti6Al4V material. *Int J Adv Manuf Technol* 97(1-4):495–510
12. Gümrük R, Mines RAW, Karadeniz S (2018) Determination of strain rate sensitivity of micro-struts manufactured using the selective laser melting method. *J Mater Eng Perform* 27(3):1016–1032
 13. Demir AG, Colombo P, Previtali B (2017) From pulsed to continuous wave emission in SLM with contemporary fiber laser sources: effect of temporal and spatial pulse overlap in part quality. *Int J Adv Manuf Technol* 91(5-8):2701–2714
 14. Lee J, Choe J, Park J, Yu J-H, Kim S, Jung ID, Sung H (2019) Microstructural effects on the tensile and fracture behavior of selective laser melted H13 tool steel under varying conditions. *Mater Charact* 155:109817
 15. Ren B, Lu D, Zhou R, Li Z, Guan J (2019) Preparation and mechanical properties of selective laser melted H13 steel. *J Mater Res* 34(08):1415–1425
 16. Reggiani B, Todaro I (2019) Investigation on the design of a novel selective laser melted insert for extrusion dies with conformal cooling channels. *Int J Adv Manuf Technol* 104(1-4):815–830
 17. Nguyen VL, Kim E-a, Yun J, Choe J, Yang D-y, Lee H-s, Lee C-w, Yu J-H (2018) Nano-mechanical behavior of H13 tool steel fabricated by a selective laser melting method. *Metall Mater Trans A* 50(2):523–528
 18. Narvan M, Al-Rubaie KS, Elbestawi M (2019) Process-structure-property relationships of AISI H13 tool steel processed with selective laser melting. *Materials (Basel)* 12:(14).
 19. Chen H, Gu D, Dai D, Ma C, Xia M (2017) Microstructure and composition homogeneity, tensile property, and underlying thermal physical mechanism of selective laser melting tool steel parts. *Mater Sci Eng A* 682:279–289
 20. Torres RD, Soares PC, Schmitz C, Siqueira CJM (2010) Influence of the nitriding and TiAlN/TiN coating thickness on the sliding wear behavior of duplex treated AISI H13 steel. *Surf Coat Technol* 205(5):1381–1385
 21. Castro G, Fernández-Vicente A, Cid J (2007) Influence of the nitriding time in the wear behaviour of an AISI H13 steel during a crankshaft forging process. *Wear* 263(7-12):1375–1385
 22. Kariofillis GK, Kiourtsidis GE, Tsiapas DN (2006) Corrosion behavior of borided AISI H13 hot work steel. *Surf Coat Technol* 201(1-2):19–24
 23. Qin Q, Chen GX (2013) Microstructure and mechanical property analysis of the metal part by SLM. *Appl Mech Mater* 423-426:693–698
 24. Mertens R, Vrancken B, Holmstock N, Kinds Y, Kruth JP, Van Humbeek J (2016) Influence of powder bed preheating on microstructure and mechanical properties of H13 tool steel SLM parts. *Phys Procedia* 83:882–890
 25. Lee J-H, Jang J-H, Joo B-D, Son Y-M, Moon Y-H (2009) Laser surface hardening of AISI H13 tool steel. *Trans Nonferrous Metals Soc China* 19(4):917–920
 26. Du Y, Liu XH, Fu B, Shaw TM, Lu M, Wassick TA, Bonilla G, Lu H (2016) Creep characterization of solder bumps using nanoindentation. *Mech Time-Dependent Mater* 21(3):287–305
 27. Papadakis L, Chantzis D, Salonitis K (2017) On the energy efficiency of pre-heating methods in SLM/SLS processes. *Int J Adv Manuf Technol* 95(1-4):1325–1338
 28. Kurzynowski T, Stopyra W, Gruber K, Ziolkowski G, Kuznicka B, Chlebus E (2019) Effect of scanning and support strategies on relative density of SLM-ed H13 steel in relation to specimens size. *Materials (Basel)* 12:(2)
 29. Jung ID, Choe J, Yun J, Yang S, Yang DY, Kim YJ, & Yu JH (2019) Dual speed laser remelting for high densification in H13 tool steel metal 3D Printing.pdf. *Arch Metall Mater* 64.
 30. Rami A, Kallel A, Djemaa S, Mabrouki T, Sghaier S, Hamdi H (2018) Numerical assessment of residual stresses induced by combining turning-burnishing (CoTuB) process of AISI 4140 steel using 3D simulation based on a mixed approach. *Int J Adv Manuf Technol* 97(5-8):1897–1912
 31. Gu D, Hagedorn Y-C, Meiners W, Meng G, Batista RJS, Wissenbach K, Poprawe R (2012) Densification behavior, microstructure evolution, and wear performance of selective laser melting processed commercially pure titanium. *Acta Mater* 60(9):3849–3860
 32. Attar H, K. G. P, Chaubey AK, Calin M (2014) Comparison of wear properties of commercially pure titanium prepared by selective laser melting. *Mater Lett* 142:38–41
 33. AlMangour B, Grzesiak D, Yang J-M (2017) Selective laser melting of TiB 2/H13 steel nanocomposites: influence of hot isostatic pressing post-treatment. *J Mater Process Technol* 244:344–353
 34. Saeidi K, Gao X, Lofaj F, Kvetková L, Shen ZJ (2015) Transformation of austenite to duplex austenite-ferrite assembly in annealed stainless steel 316L consolidated by laser melting. *J Alloys Compd* 633:463–469
 35. Yan JJ, Zheng DL, Li HX, Jia X, Sun JF, Li YL, Qian M, Yan M (2017) Selective laser melting of H13: microstructure and residual stress. *J Mater Sci* 52(20):12476–12485
 36. Chen H, Gu D, Dai D, Xia M, Ma C (2018) A novel approach to direct preparation of complete lath martensite microstructure in tool steel by selective laser melting. *Mater Lett* 227:128–131
 37. Deirmina F, AlMangour B, Grzesiak D, Pellizzari M (2018) H13–partially stabilized zirconia nanocomposites fabricated by high-energy mechanical milling and selective laser melting. *Mater Des* 146:286–297
 38. Azizi H, Ghiaasiaan R, Prager R, Ghoncheh MH, Samk KA, Lausic A, Byleveld W, Phillion AB (2019) Metallurgical and mechanical assessment of hybrid additively-manufactured maraging tool steels via selective laser melting. *Addit Manuf* 27:389–397
 39. Mertens RVB, Holmstock N, Kinds Y, Kruth JP (2016) Influence of powder bed preheating on microstructure and mechanical properties of H13 tool steel SLM parts. *Phys Procedia* 83:882–890
 40. Nguyen V, Kim E-a, Lee S.-R, Yun J, Choe J, Yang D-y, Lee, H.-s, Lee, C.-w, Yu J.-H. (2018) Evaluation of strain-rate sensitivity of selective laser melted H13 tool steel using nanoindentation tests. *Metals* 8(8).
 41. Wang M, Li W, Wu Y, Li S, Cai C, Wen S, Wei Q, Shi Y, Ye F, Chen Z (2018) High-temperature properties and microstructural stability of the AISI H13 hot-work tool steel processed by selective laser melting. *Metall Mater Trans B* 50(1):531–542
 42. AlMangour B, Grzesiak D, Yang J-M (2016) Nanocrystalline TiC-reinforced H13 steel matrix nanocomposites fabricated by selective laser melting. *Mater Des* 96:150–161
 43. AlMangour B, Yu F, Yang J-M, Grzesiak D (2017) Selective laser melting of TiC/H13 steel bulk-form nanocomposites with variations in processing parameters. *MRS Communications* 7(1):84–89
 44. Fischer P, Romano V, Weber HP, Karapatis NP, Boillat E, Gardon R (2003) Sintering of commercially pure titanium powder with a Nd:YAG laser source. *Acta Mater* 51(6):1651–1662
 45. Harrison NJ, Todd I, Mumtaz K (2015) Reduction of microcracking in nickel superalloys processed by Selective Laser Melting: a fundamental alloy design approach. *Acta Mater* 94:59–68
 46. Garibaldi M, Ashcroft I, Simonelli M, Hague R (2016) Metallurgy of high-silicon steel parts produced using Selective Laser Melting. *Acta Mater* 110:207–216
 47. Thijs L, Verhaeghe F, Craeghs T, Humbeek JV, Kruth J-P (2010) A study of the microstructural evolution during selective laser melting of Ti–6Al–4 V. *Acta Mater* 58(9):3303–3312
 48. Primig S, Leitner H (2011) Separation of overlapping retained austenite decomposition and cementite precipitation reactions during tempering of martensitic steel by means of thermal analysis. *Thermochim Acta* 526(1-2):111–117

49. Mazur M, Brincat P, Leary M, Brandt M (2017) Numerical and experimental evaluation of a conformally cooled H13 steel injection mould manufactured with selective laser melting. *Int J Adv Manuf Technol* 93(1-4):881–900
50. Taheri H, Shoaib MRBM, Koester LW, Bigelow TA, Collins PC; Bond LJ (2017) Powder-based additive manufacturing—a review of types of defects, generation mechanisms, detection, property evaluation and metrology. *International Journal of Additive and Subtractive Materials Manufacturing* 1(2).
51. Kempen KVB, Buls S, Thijs L, Van Humbeeck J, Kruth JP (2014) Selective laser melting of crack-free high density M2 high speed steel parts by baseplate preheating. *Manuf SciEng*:136
52. Gu D, Shen Y (2009) Balling phenomena in direct laser sintering of stainless steel powder: metallurgical mechanisms and control methods. *Mater Des* 30(8):2903–2910
53. Kruth JPFL, Van Vaerenbergh, J, Mercelis P, Rombouts M, Lauwers B (2004) Selective laser melting of iron-based powder. *Mater Process Technol* 149, (616–622).
54. Zhang B, Liao H, Coddet C (2012) Effects of processing parameters on properties of selective laser melting Mg–9%Al powder mixture. *Mater Des* 34:753–758
55. Khan M, Dickens P (2010) Selective laser melting (SLM) of pure gold. *onAcademic* 43(2):114–121
56. Wang L-z, Wang S, Wu J-j (2017) Experimental investigation on densification behavior and surface roughness of AlSi10Mg powders produced by selective laser melting. *Opt Laser Technol* 96:88–96
57. Zhang J, Song B, Wei Q, Bourell D, Shi Y (2019) A review of selective laser melting of aluminum alloys: processing, microstructure, property and developing trends. *J Mater Sci Technol* 35(2): 270–284
58. Mukesh Agarwala DB, Beaman J, Marcus H, Barlow J (1995) Direct selective laser sintering of metals. *Rapid Prototyp J* 1:26–36
59. Saeidi K, Gao X, Zhong Y, Shen ZJ (2015) Hardened austenite steel with columnar sub-grain structure formed by laser melting. *Mater Sci Eng A* 625:221–229
60. Deirmina F, Peghini N, AlMangour B, Grzesiak D, Pellizzari M (2019) Heat treatment and properties of a hot work tool steel fabricated by additive manufacturing. *Mater Sci Eng A* 753:109–121
61. Ackermann M, Šafka J, Voleský L, Bobek J, Kondapally JR (2018) Impact testing of H13 tool steel processed with use of selective laser melting technology. *Mater Sci Forum* 919:43–51
62. Joo B-D, Jang J-H, Lee J-H, Son Y-M, Moon Y-H (2009) Selective laser melting of Fe-Ni-Cr layer on AISI H13 tool steel. *Trans Nonferrous Metals Soc China* 19(4):921–924
63. Dadbakhsh S, Hao L (2012) Effect of hot isostatic pressing (HIP) on Al composite parts made from laser consolidated Al/Fe₂O₃ powder mixtures. *J Mater Process Technol* 212(11):2474–2483
64. Simchi A (2004) Asgharzadeh, H. Densification and microstructural evaluation during laser sintering of m2 high speed steel powder. *Mater Sci Technol* 20(11):1462–1468
65. Santos L, de Jesus J, Ferreira J, Costa J, Capela C (2018) Fracture toughness of hybrid components with selective laser melting 18Ni300 steel parts. *Appl Sci* 8(10).
66. Badrossamay M, Childs THC (2007) Further studies in selective laser melting of stainless and tool steel powders. *Int J Mach Tools Manuf* 47(5):779–784
67. Holzweissig MJ, Taube A, Brenne F, Schaper M, Niendorf T (2015) Microstructural characterization and mechanical performance of hot work tool steel processed by selective laser melting. *Metall Mater Trans B* 46(2):545–549
68. Zhang JSB, Wei Q, Bourell D (2019) A review of selective laser melting of aluminum alloys: processing, microstructure, property and developing trends. *J Mater Sci Technol* 35(2):270–284
69. Yadroitsev I, Gusarov A, Yadroitsava I, Smurov I (2010) Single track formation in selective laser melting of metal powders. *J Mater Process Technol* 210(12):1624–1631
70. Breidenstein B, Brenne F, Wu L, Niendorf T, Denkena B (2018) Effect of post-process machining on surface properties of additively manufactured H13 tool steel. *HTM J Heat Treatment Mater* 73(4): 173–186
71. Tong X, Dai M-j, Zhang Z-h (2013) Thermal fatigue resistance of H13 steel treated by selective laser surface melting and CrNi alloying. *Appl Surf Sci* 271:373–380
72. Körperich JP, Merkel M (2018) Thermographic analysis of the building height impact on the properties of tool steel in selective laser beam melting. *Mater Werkst* 49(5):689–695

Publisher's note Springer Nature remains neutral with regard to jurisdictional claims in published maps and institutional affiliations.